Multifrequency measurements of core-diffracted P waves (Pdiff) for global waveform tomography

Kasra Hosseini, Karin Sigloch

Geophysical Journal International

Geophys. J. Int. (2015) **203,** 506–521 doi: 10.1093/gji/ggv298
GJI Seismology

Multifrequency measurements of core-diffracted *P* waves (Pdiff) for global waveform tomography

Kasra Hosseini[1] and Karin Sigloch[2]

[1]*Department of Earth Sciences, Ludwig-Maximilians-Universität München, Theresienstrasse* 41*, D-*80333 *Munich, Germany.*
E-mail: hosseini@geophysik.uni-muenchen.de
[2]*Department of Earth Sciences, University of Oxford, South Parks Road, Oxford* OX1 3AN*, UK*

Accepted 2015 July 14. Received 2015 June 30; in original form 2015 April 4

SUMMARY

The lower third of the mantle is sampled extensively by body waves that diffract around the earth's core (Pdiff and Sdiff phases), which could deliver highly resolved tomographic images of this poorly understood region. But core-diffracted waves—especially Pdiff waves—are not often used in tomography because they are difficult to model adequately. Our aim is to make core-diffracted body waves usable for global waveform tomography, across their entire frequency range. Here we present the data processing part of this effort. A method is demonstrated that routinely calculates finite-frequency traveltimes of Pdiff waves by cross-correlating large quantities of waveform data with synthetic seismograms, in frequency passbands ranging from 30.0 to 2.7 s dominant period. Green's functions for 1857 earthquakes, typically comprising thousands of seismograms, are calculated by theoretically exact wave propagation through a spherically symmetric earth model, up to 1 Hz dominant period. Out of 418 226 candidates, 165 651 (39.6 per cent) source–receiver pairs yielded at least one successful passband measurement of a Pdiff traveltime anomaly, for a total of 479 559 traveltimes in the eight passbands considered. Measurements of teleseismic *P* waves yielded 448 178 usable source–receiver paths from 613 057 candidates (73.1 per cent success rate), for a total of 2 306 755 usable teleseismic dT in eight passbands. Observed and predicted characteristics of Pdiff traveltimes are discussed and compared to teleseismic *P* for this very large data set. Pdiff measurements are noise-limited due to severe wave attenuation with epicentral distance and frequency. Measurement success drops from 40–60 per cent at 80° distance, to 5–10 per cent at 140°. Frequency has a 2–3 times stronger influence on measurement success for Pdiff than for *P*. The fewest usable dT measurements are obtained in the microseismic noise band, whereas the fewest usable teleseismic *P* measurements occur at the highest frequencies. dT anomalies are larger for Pdiff than for *P*, and frequency dependence of dT due to 3-D heterogeneity (rather than just diffraction) is larger for Pdiff as well. Projecting the Pdiff traveltime anomalies on their core-grazing segments, we retrieve well-known, large-scale structural heterogeneities of the lowermost mantle, such as the two Large Low Shear Velocity Provinces, an Ultra-Low Velocity Zone west of Hawaii, and subducted slab accumulations under East Asia and Central America.

Key words: Time-series analysis; Numerical solutions; Body waves; Seismic tomography; Wave scattering and diffraction; Wave propagation.

1 INTRODUCTION

Core-diffracted waves are seismic body waves that dive deep enough to sense the earth's core, and by interaction with this boundary become dispersive. In ray-theoretical modelling, the transition from teleseismic to core-diffracted wave occurs at the epicentral distance where the deepest ray segment no longer turns in the mantle, but starts to graze the core–mantle boundary (CMB). For *P* waves, this happens at ≈98° epicentral distance if source and receiver are located near the surface. In reality, ray theory is a poor approximation of the true, finite-frequency sensitivity of a core-diffracted wave, which resembles a spatially extended banana in the mantle, but flattens elliptically on top of the CMB due to diffraction (Liu & Tromp 2008). Actual body waves already sense the core when the banana's lower lobe extends to the CMB, which happens at significantly smaller distances than 98°.

Core-diffracted waves, and Pdiff waves in particular, have been used to study lowermost mantle structure (Su & Dziewonski 1997;

Masters *et al.* 2000; Ritsema & van Heijst 2002; Li *et al.* 2008), but they have seen very little use in tomography, despite being the most highly resolving wave type that extensively samples the lower third of the mantle. The problem is that modelling their wave propagation and non-ray-like sensitivities to a reasonable approximation is challenging, requiring computationally expensive forward modelling techniques. Global *P*-wave tomographies often include data in the far teleseismic range, which effectively start to sense the core (generally neglected by the sensitivity modelling), but they stop short of including 'real' Pdiff data. Sparser sampling and poorer modelling result in coarser image resolution and significant discrepancies across tomographic models, even for large-scale features. Hence, our knowledge of structural detail in the lowermost mantle is lacking compared to shallower levels. For example, many regional and global tomographies have proposed detailed tectonic or paleogeographic interpretations of slab geometries imaged at upper and mid mantle depths (e.g. for Tethyan slabs: Van der Voo *et al.* (1999b); Hafkenscheid *et al.* (2006); for North America: Grand (2002); Ren *et al.* (2007); Pavlis *et al.* (2012); Sigloch & Mihalynuk (2013); globally: Li *et al.* (2008); van der Meer *et al.* (2010)). The same has rarely been attempted for slabs in the lower third of the mantle (Van der Voo *et al.* 1999a; van der Meer *et al.* 2010), despite agreement between virtually all global tomography models that extensive fast-velocity provinces are present at these depths.

To our knowledge, the only global *P*-wave tomographies to explicitly model and include Pdiff traveltime data were by Wysession (1996) and Kàrason & Van der Hilst (2001), both using a set of 543 differential Pdiff-PKP measurements. Wysession (1996) treated the mantle path by ray theory and sensitivity at the CMB by an approximate elliptical Fresnel zone of constant value. Kàrason & Van der Hilst (2001) improved on this by constructing approximate 3-D sensitivity kernels instead of assuming a constant Fresnel zone, and inverted for 3-D mantle structure rather than a 2-D map of velocity anomalies on the CMB. Resolution was obviously limited with only 543 measurements (compared to half a million presented here). The same kernels and data set were reused by Li *et al.* (2008).

A few global *S*-wave tomographies explicitly include Sdiff data. Ritsema *et al.* (2004, 2011) include cross-correlation traveltime measurements of *SH*-diff waves and model them by ray-theoretical sensitivities. Mégnin & Romanowicz (2000) and Panning & Romanowicz (2006) include *SH*-diff data in their waveform inversion, modelling sensitivities by mode coupling in the NACT approximation, which features spatially extended sensitivities in the source–receiver plane, but no sensitivity perpendicular to it. Wave periods in these models were limited to 30 s and longer.

Most global tomographies include non-diffracted wave types that sample the lowermost mantle, for example, core phases, core-reflected phases, long-range teleseismic waves near the diffraction limit, or normal modes. The structural findings from these data have converged robustly on certain very large scale features in the lower mantle, such as Large Low Shear Velocity Provinces (e.g. Woodhouse & Dziewonski 1989; Masters *et al.* 2000; Mégnin & Romanowicz 2000; Grand 2002; Ritsema & van Heijst 2002; Montelli *et al.* 2006), but resolution remains limited by the long wavelengths used and/or by modelling mismatches inherent in using approximate sensitivities.

We aim to improve on the state of the art as follows:

(1) Model and measure core-diffracted body waves across their entire spectrum, up to the highest occurring frequencies. The goal is maximum spatial resolution.

(2) 'No data left behind': a processing strategy efficient enough to assemble the largest possible data sets (Hosseini-zad *et al.* 2012).

(3) Use of Pdiff in addition to Sdiff.

(4) Better approximation of true wave sensitivities by 3-D Born-Fréchet kernels.

Items 1 and 2 aim for maximum spatial resolution and coverage globally. In terms of wave type, we started with Pdiff because it will integrate seamlessly with our teleseismic *P*-wave inversions, but the processing methods presented here carry over to Sdiff with only minimal changes. For the ambitious data volumes, frequencies and distances targeted, fully numerical modelling in global 3-D reference models (e.g. Komatitsch & Tromp 2002a) remains well beyond reach, but the semi-analytical modelling of 3-D wave fields and sensitivities in spherically symmetric earth models is becoming feasible. We discuss the forward modelling of core-diffracted seismograms, deferring the calculation of Born-Fréchet sensitivity kernels to a later paper.

Section 2.1 introduces the observational characteristics of Pdiff waves: strong dispersion and attenuation as functions of frequency and epicentral distance. Section 2.2 describes our successful adoption of two recent numerical packages for computing broad-band Green's functions: *Yspec* (Al-Attar & Woodhouse 2008) and *AxiSEM* (Nissen-Meyer *et al.* 2014). In practice, the success of fitting broad-band waveforms depends not only on accurate Green's functions but equally on reliable estimates of source time functions and source depths. We compute traveltime measurements by cross-correlation in multiple frequency bands—essentially frequency-dependent phase shifts. Section 3 analyses the global data set of multifrequency traveltimes obtained so far: 479 559 *P*-diffracted and 2 306 755 teleseismic *P* measurements. We discuss how measurement success depends on epicentral distance, frequency band and earthquake magnitude. The statistics of traveltimes for Pdiff and teleseismic *P* are presented, including their frequency dependence. The information content of the novel Pdiff measurements is demonstrated by projecting traveltime anomalies on the core-grazing segments of their nominal ray paths. Already from this 'proto-tomography' exercise, structural heterogeneity of considerable detail emerges, which in Section 4 is compared to current structural knowledge about the lowermost mantle.

2 WAVEFORM DATA AND PROCESSING METHODS

2.1 Waveform recordings of core-diffracted *P* waves

We start by discussing the nature of *P*-diffracted waves. As the travel distance of a teleseismic *P* wave increases and transitions into the core-diffracted regime, the character of the waveform changes. Fig. 1 illustrates this for broad-band data from a deep earthquake of magnitude 7.5 in Southern Sumatra (2009/09/30 10:16:09, 0.72°S, 99.87°E, depth: 82.0 km). Sharply defined pulses recorded in the teleseismic distance range ($\Delta < 90°$) morph into increasingly emergent oscillations at distances exceeding 100°. This is clearly observable for the isolated (blue) *P* pulse arrival in the real data (Fig. 1a), and even more evident in the modelled Green's functions of Fig. 1(c). (Broad-band Green's functions were computed with the *Yspec* software of Al-Attar & Woodhouse (2008), described in Section 2.2.) At ranges $\Delta < 100°$, two surface phases pP and sP (in red) are clearly distinguished 20–40 s after the *P* arrival, whereas in the Pdiff range these two pulses are smeared together. In other words, high-frequency content is lost disproportionately with

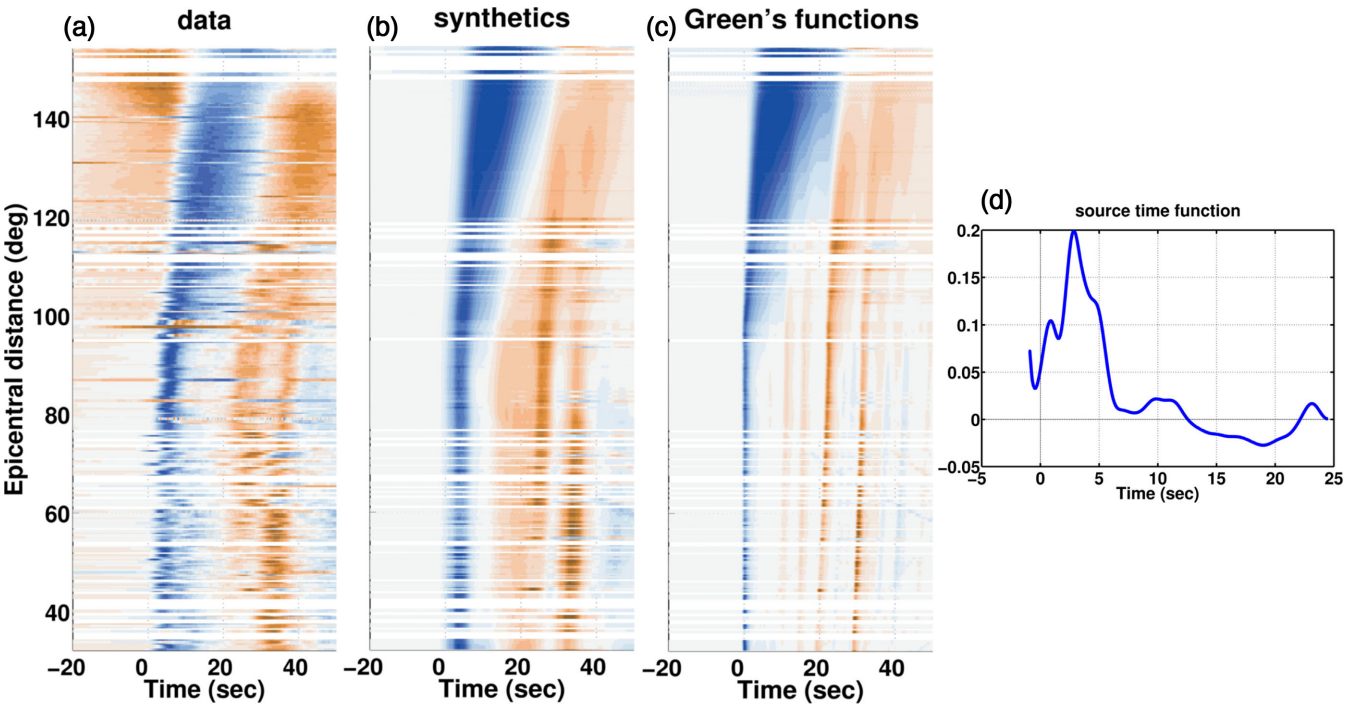

Figure 1. Observed versus modelled broad-band seismograms of teleseismic and core-diffracted *P* waves. Record section of a deep magnitude 7.5 earthquake in Southern Sumatra (2009/09/30 10:16:09.2, at 0.72°S, 99.87°E, 82 km depth), recorded on seismic networks globally. (a) Observed broad-band waveforms aligned on their ray-theoretical *P*-arrival times. Each line shows a seismogram (vertical component) of normalized RMS amplitude, from 20 s before to 50 s after *P* arrival; positive samples are blue, negative samples are red. Waveforms include the direct *P* phase (blue), and in its wake the pP and sP surface reflections (red). The Pdiff epicentral distance range >120° is particularly densely sampled by several hundred USArray stations. The increasingly broad and emergent pulses beyond distances of 100° result from diffraction around the earth's core. Red samples preceding the *P* arrival are a filter response resulting from highpass filtering at 100 s corner period, which serves to suppress low-frequency noise. (b) Broad-band synthetics, the convolution of the Green's functions in panel (c) with the source time function in panel (d). (c) Broad-band Green's functions (up to 1 Hz dominant period) computed in a spherically symmetric earth model by the *Yspec* method of Al-Attar & Woodhouse (2008). (d) The broad-band source time function (amplitude normalized), which was deconvolved from panels (a) and (c).

distance in the core-diffracted range, while this is not the case in the teleseismic range. The increasingly emergent and low passed character of the Pdiff pulses in Figs 1(a)–(c) indicates that ray-theoretical processing methods such as manual or automated onset picking would be inadequate because they rely on sharp, impulsive onsets. The emergent onsets are a manifestation of the different physics of diffracted wave propagation, for which the ray-theoretical approximation breaks down.

The dependence of wave amplitude on source–receiver distance is not apparent in Fig. 1 because each trace is energy-normalized, but it differs fundamentally between *P* and Pdiff (Knopoff & Gilbert 1961; Sacks 1966). In a computational experiment, we calculated broad-band Green's functions as in Fig. 1(c), except that an explosive source was used, 100 km deep in order to cleanly isolate the *P* pulse from its echoes. The vertical component waveforms were filtered to eight overlapping frequency passbands with dominant periods ranging from 30.0 to 2.7 s. (The filters are used throughout this study and described in Section 2.3.2.) RMS amplitudes of the bandpassed Green's functions were measured at epicentral distances from 40° to 150° in increments of 1°.

Fig. 2 shows the result: with increasing travel distance, amplitudes drop much more severely for Pdiff than for *P*. This is true in any frequency band, but particularly pronounced for high frequencies. Straight lines in this lin-log plot indicate exponential loss of energy with distance, the negative line slope being the attenuation constant in the exponent. Slopes in the *P*-diffracted range are steep and strongly dispersive—in the far Pdiff range, higher frequencies can be suppressed by orders of magnitude. This creates a signal-to-noise challenge for Pdiff measurements, and Section 3.1 investigates its practical consequences.

The Pdiff slopes of Fig. 2 are found to be in good agreement with analytical predictions of (Aki & Richards 2002, p. 457), superimposed as dash-dotted lines. They predict the amplitude A of core-diffracted *P* waves to be proportional to

$$A \propto \exp\left[-\omega^{1/3}\lambda \sin(\pi/3)(\Delta_0 - \Delta_d)\right], \quad (1)$$

where ω is the angular frequency, λ is a positive constant and Δ_0 is the source–receiver distance. In the teleseismic range, the *P* and PcP pulses approach each other in time with increasing Δ_0 until they merge at Δ_d, which is called the shadow boundary. Beyond Δ_d, the rays start to creep around the CMB as diffracted *P* waves. With increasing frequency and/or distance (both in the exponent), the wave amplitude of Pdiff attenuates rapidly. To create the dash-dotted lines in Fig. 2, we estimated the constant λ by fitting above analytical solution to our results for the highest frequency band (2.7 s). This λ value was then used to calculate slopes for the other two frequency bands (5.3 s and 10.6 s), and the result is very consistent with the prediction.

Compared to the core-diffracted distance range, amplitude decrease in the teleseismic range is moderate, caused mainly by geometrical spreading. Intrinsic attenuation—in the real earth and in this simulation—does cause exponential loss of amplitude with travel distance and with frequency, but in practice the effect is mild

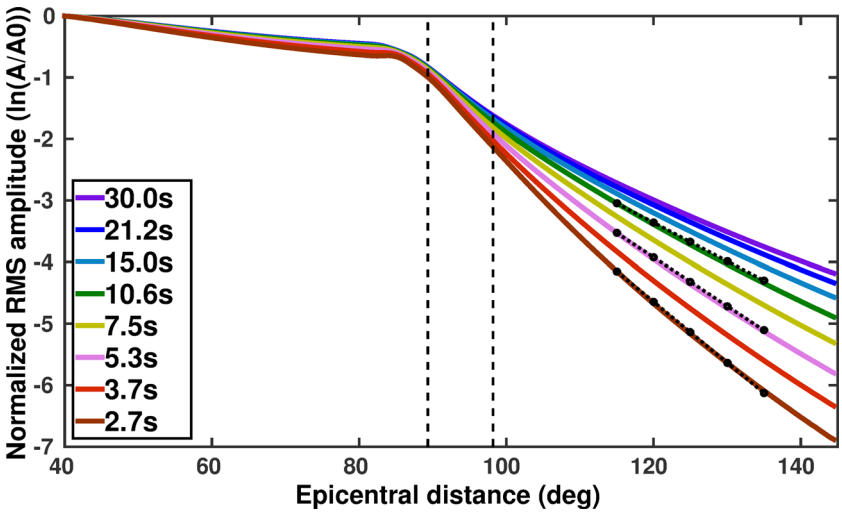

Figure 2. *P*-diffracted waves are highly attenuative and dispersive compared to teleseismic *P* waves—the effect of diffraction around the earth's core. As a function of epicentral distance, the logarithmic RMS amplitudes $\ln(A/A_0)$ of Green's functions are plotted. (Explosive source, 100 km deep, vertical receiver component, computed up to 1 s dominant period in velocity model IASP91 including PREM attenuation.) Coloured lines distinguish eight frequency passbands, labelled by their dominant periods. Amplitudes A in each band are normalized to the amplitude A_0 of a *P* wave at 40° distance. In this lin-log plot, straight lines indicate exponential loss of wave amplitude with distance, and negative line slopes represent the attenuation constants in the exponent. Divergence of coloured lines in the Pdiff range indicates frequency dispersion. Dash-dotted slopes are ray-theoretical predictions (Aki & Richards 2002, p. 457), vertical dashed lines predict the distances at which a ray-theoretical *P* wave would first hit the D'' and the CMB, respectively.

(the coloured lines barely diverge), thanks to relatively low intrinsic attenuation in the mantle.

The transition from the *P* to the Pdiff regime in Fig. 2 occurs at a significantly smaller distance than predicted by ray theory. The second dashed line, around 98°, marks the predicted onset of core-grazing rays for the deep source depth used (100 km depth). However, waves in our physically more realistic simulation have volumetrically extended, banana-like sensitivities to mantle structure, and start to sense the core at distances as small as 85°. 'Teleseismic' waves at those distances are not well modelled by ray theory.

2.2 Modelling core-diffracted waves

Broad-band waveform tomography on a global scale has three modelling requirements:

(1) Green's functions;
(2) source time functions;
(3) sensitivity kernels.

The main obstacle to exploiting core-diffracted waves has been modelling them to a sufficiently realistic degree. We employ recently developed, semi-analytical tools for forward wave propagation and discuss the computation of Green's functions and source time functions. Sensitivity kernels are required for inversion of the data in a linearized optimization problem. (Unless global search approaches are used, which only rely on a large number of forward calculations but are computationally out of reach for the number of parameters required in 3-D inversions.) Tomographic inversion of our Pdiff data will be the topic of a follow-up paper, but we briefly discuss how the numerical tools for Green's function and kernel computations relate.

An observed seismogram is the convolution of an earthquake's source time function with the earth's Green's function between a given source–receiver pair. Waveform tomography compares this to a predicted seismogram, which is a Green's function computed in a reference earth model convolved with an estimate of the earthquake's source time function. Fig. 1 shows a typical broad-band data example for observed seismograms (Fig. 1a) and their predicted counterparts (Fig. 1b), which in turn are the convolution of the computed Green's functions (Fig. 1c) with a source time function estimate (Fig. 1d).

2.3 Green's functions

We compute Green's functions by simulating wave propagation in a broad-banded spectrum from 0.2 mHz to 1 Hz in the spherically symmetric earth model IASP91 (Kennett & Engdahl 1991) with density and attenuation from PREM (Dziewonski & Anderson 1981).

Two numerical software packages are suitable for these calculations: *Yspec* (Al-Attar & Woodhouse 2008) and *AxiSEM* (Nissen-Meyer *et al.* 2007, 2014). *Yspec* is very efficient for calculating synthetic seismograms in spherically symmetric earth models using the direct radial integration method (Woodhouse 1980; Friederich & Dalkolmo 1995), which can account for the full physics of such media including viscoelastic damping (used here) and transverse isotropy (not used here). *AxiSEM* is a spectral-element code that computes 3-D global seismic wavefields for full moment tensor sources in viscoelastic (van Driel & Nissen-Meyer 2014a), anisotropic (van Driel & Nissen-Meyer 2014b) media across the observable frequency band at a reasonable computational cost.

Both *Yspec* and *AxiSEM* are semi-analytical methods that solve the full physics of wave propagation, but make use of the earth model's assumed spherical symmetry to analytically reduce the cost of computing 3-D wavefields—as compared to fully numerical simulations of wave propagation in 3-D heterogeneous earth models (e.g. Komatitsch & Tromp 2002a; Fichtner *et al.* 2009). Aside from numerical imprecisions, either approach computes 3-D wavefields that are theoretically exact within its modelling assumptions, but only the semi-analytical computations are efficient enough for our application.

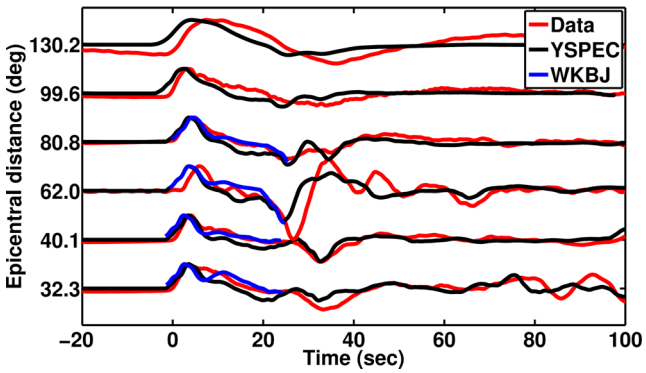

Figure 3. Broad-band waveform modelling, a comparison of methods for selected seismograms of the Sumatra event in Fig. 1. All synthetics for this study were computed by the semi-analytical *Yspec* software of Al-Attar & Woodhouse (2008) (in black) to a dominant period of 1 s. Our previous teleseismic studies used the asymptotic WKBJ method (blue), which is seen to be broadly consistent, but differs in detail and is not suited to computing core-diffracted waveforms. The broad-band observations are shown in red.

Yspec and *AxiSEM* have been benchmarked against each other between 1 mHz and 1 Hz, yielding virtually indistinguishable seismograms (Nissen-Meyer *et al.* 2014). Since the implementation of attenuation and anisotropy in *AxiSEM* were not yet complete, all traces in this study were calculated with *Yspec*, which was very efficient for our forward modelling purposes. An example of its broad-band Green's functions is shown in Fig. 1(c). *Yspec* took ≈480 CPU hours for our typical event of ≈3000 seismograms (1000 stations, 3 components), up to a dominant frequency of 1 Hz. This is an order of magnitude faster than *AxiSEM* for a single event. Computation scaled linearly with the number of sources, and we computed 2000 earthquakes for this study, expending a total of $\approx 10^6$ CPU hours. Sensitivity kernels are much more expensive to compute than Green's functions. For our present application, only *AxiSEM* is suitable for sensitivity kernel calculations thanks to its efficiency in computing and storing the spatiotemporal evolution of the 3-D wavefields. Hence, for the inversion stage we will switch to *AxiSEM*.

AxiSEM and *Yspec* are semi-analytical, theoretically exact methods that include the full physics of wave propagation but exploit (spherical) symmetry in the background model for efficient computation. By contrast, our earlier studies used asymptotic (and therefore approximate) forward modelling methods, also assuming spherical symmetry. For teleseismic *P* measurements, Sigloch & Nolet (2006) used the WKBJ method of Chapman (1978); and for triplicated body waves, Stähler *et al.* (2012) used the reflectivity method by Fuchs & Müller (1971). Fig. 3 compares broad-band observations, WKBJ synthetics and *Yspec* synthetics for the Sumatra event of Fig. 1. While agreeing in their basic characteristics, there are clear differences between WKBJ and *Yspec* synthetics in the teleseismic range, where both are applicable. (WKBJ does not compute core-diffracted waves.) Differences between *AxiSEM* and *Yspec* are much smaller (Nissen-Meyer *et al.* 2014) than the difference between *Yspec* and the asymptotic WKBJ method.

2.3.1 Source time functions

For fitting waveforms at the high frequencies included here, equally important as Green's functions are good estimates of earthquake source parameters, especially depth and source time function. This becomes clear on the data example of Fig. 1. Source depth determines the temporal spacing of the P, pP and sP pulses, a nonlinear effect that affects all frequency bands and is pronounced in practice, as depth estimates from earthquake catalogues are afflicted by large uncertainties. The source time function broadens and modulates the pulses—in this case, a ≈7 s long source time function convolves pulses spaced by about 20 s (P and pP) or 10 s (pP and sP), see Figs 1(c) versus (b). This is the benign case of a 82-km deep earthquake, but most sources are shallower and their depth phases are smeared together by the source wavelet, in practice affecting all frequency bands of relevance to us.

No earthquake catalogue has been delivering source time function estimates, and hence we expend a significant effort on deconvolving them from data and Green's functions, in a linearized procedure described by Sigloch & Nolet (2006). For this study, source time functions for 1857 events since 1999 were deconvolved from teleseismic *P* waves and were subsequently used to calculate predicted seismograms at all distance ranges. As an important side benefit, this yields significantly more confident depth estimates than routine catalogue determinations—a parameter of great importance even for waveform tomography at relatively lower frequencies, where source time functions are somewhat less critical. On the downside, source deconvolution is currently the bottleneck of our processing chain because it requires the most human supervision. We are moving towards a more automated and fully probabilistic scheme (Stähler & Sigloch 2014), with the goal of producing a community catalogue of source parameters for waveform tomography. Recently, the *SCARDEC* project has been publishing an increasing number of source time function solutions for current earthquakes, using the method of Vallée *et al.* (2011). For earlier years, we have been able to compare a limited subset to our own solutions and find them to be qualitatively consistent. A quantitative comparison is ongoing.

2.3.2 Multifrequency cross-correlation traveltimes for tomography

The measurement procedure for multifrequency traveltimes is again based on that for teleseismic body waves by Sigloch & Nolet (2006). A brief summary follows, highlighting Pdiff-related adaptations.

(1) Processing proceeds earthquake by earthquake, typically on events exceeding magnitude $m_b > 5.5$. A pre-requisite is an estimate of the broad-band source time function (Section 2.3.1).

(2) A predicted broad-band seismogram or *matched filter* for a receiver *r* at an arbitrary distance range is computed by convolving its broad-band Green's function (from *Yspec* or *AxiSEM*) with the event's broad-band source time function.

(3) Broad-band observed and predicted seismograms are passed through the same filter bank of bandpass filters. We use Gabor filters in eight overlapping frequency bands, with dominant periods ranging between 30.0 and 2.7 s (Fig. 4a).

(4) The cross-correlation function between bandpassed observed and predicted waveforms is computed in each passband *b*. The time shift that maximizes this function is defined to be the *finite-frequency traveltime anomaly* $dT_{r,b}$ (Dahlen *et al.* 2000). The tomographic inversion will use these traveltime anomalies as its measure of misfit, to be minimized in a least-squares sense. $dT_{r,b}$ from all wave paths and frequency bands are required to jointly fit the (not frequency dependent) 3-D earth model solution.

Gabor filters are Gaussian functions in the log-frequency domain of constant fractional bandwidth and good spectral concentration characteristics. We space adjacent centre frequencies by $\sqrt{2}$, see Sigloch & Nolet (2006) for filter details. Figs 4(b)–(d) demonstrate

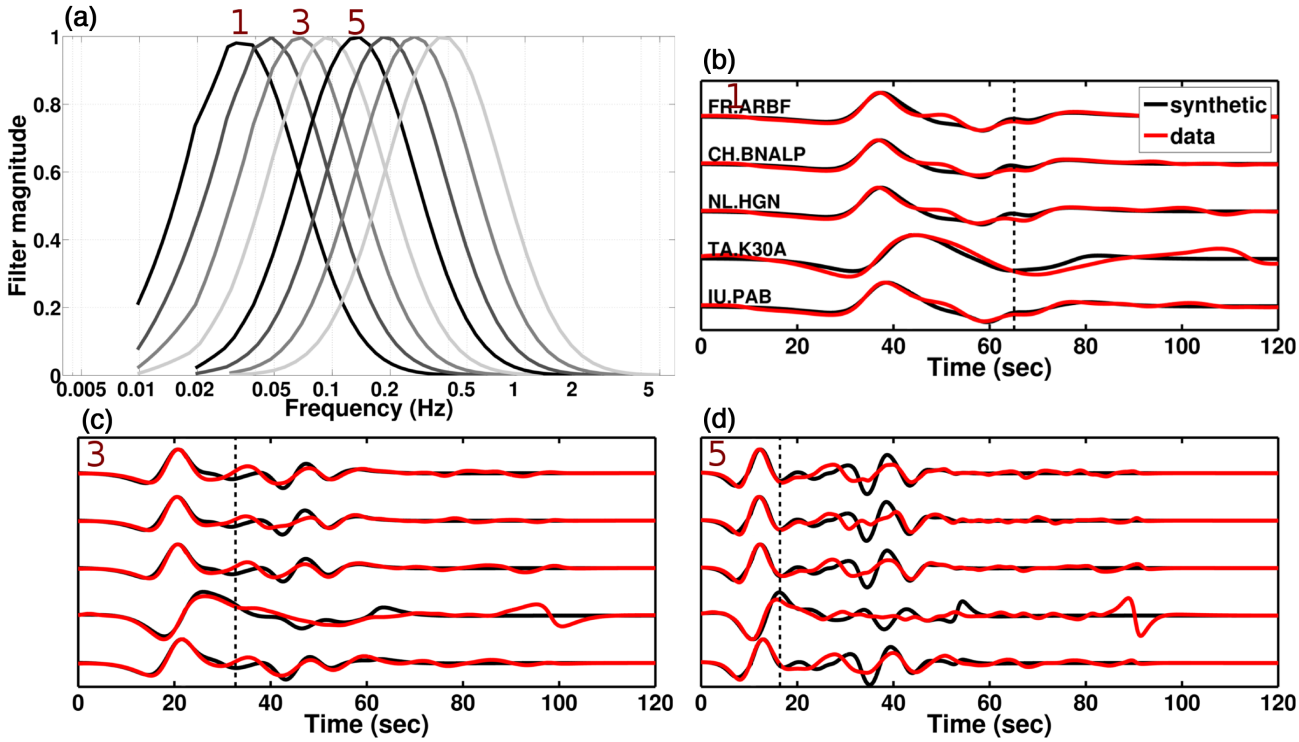

Figure 4. Procedure for multifrequency measurements of traveltimes. (a) Frequency responses of the eight bandpass filters used, Gabor filters of constant fractional bandwidth. Centre periods range from 30.0 to 2.7 s (0.033 to 0.37 Hz) and are spaced by factors of $\sqrt{2}$. (b) Selected observations (red) and *Yspec* synthetics (black) for the Sumatra event, filtered to the lowest frequency band, that is, 30.0 s dominant period. Dashed line marks 1.5 times the duration of each filter's impulse response, which we chose as the length of the correlation time window. The finite-frequency traveltime anomaly is defined as the time delay that maximizes the cross-correlation of observed and predicted waveforms within this time window. (c) Same as (b), but filtered to 15 s dominant period (band 3). (d) Same as (b), but filtered to 7.5 s dominant period (band 5).

the filtering of observed and predicted Pdiff waveforms (broad-band data from the Sumatra event of Fig. 1) to three passbands in this filter bank. We do not go beyond 2.7 s dominant period because the number of successful fits becomes very small. Hence it is effectively the nature and complexity of the real-world signal (shallow reverberations, uncertainty in source time function, etc.) that sets the upper frequency limit, rather than computational limitations (in fact our Green's functions are calculated up to 1 s dominant period).

Cross-correlation time windows are chosen as a fixed multiple of each filter's impulse response (IR) duration. Here we choose a length of 1.5*IR, marked by the vertical dashed line in Fig. 4. Empirically this choice yields robust results but other correlation window lengths are possible as long as sensitivity kernel computations mirror these choices. Cycle skipping is a potential problem in waveform cross-correlation, but we largely avoid it by first roughly aligning observed and predicted seismograms in the lowest frequency passband, and for the higher bands permitting only small time shifts relative to those initial lags. This indirectly exploits the broad-band nature of the signal to achieve more robust measurements.

As misfit measure for tomography, cross-correlation traveltimes have very favourable properties. They are robust in that cross-correlation or matched filtering is the optimal way of detecting a signal of known shape in white Gaussian noise (Sigloch & Nolet 2006, and signal processing references therein). This robustness is important in environments of high ambient noise, such as Pdiff waves at long distance ranges and high frequencies. Cross-correlation traveltimes also retain a near-linear relationship to velocity model perturbations over a larger perturbation range than direct waveform differences (samplewise *L2* misfit) (Mercerat & Nolet 2013).

2.4 Pdiff wave dispersion caused by mantle heterogeneities

Interaction with the CMB makes *P*-diffracted waves dispersive in a spherically symmetric earth, in contrast to teleseismic *P* waves. However, in a planet with lateral velocity variations, *dT* observations of teleseismic *P* waves also become dispersive, provided their wave lengths are of the same length scale as the mantle heterogeneity they interact with (Nolet & Dahlen 2000). Dispersion observed on Pdiff traveltimes will be a superposition of the two effects: diffraction around the core and finite-frequency effects caused by a 3-D heterogeneous earth.

Fig. 5 demonstrates the dispersion that arises from different spherically symmetric reference models. Besides the IASP91 model used throughout this study, we considered two models with differing velocity gradients in the D″ layer (2740–2899 km). The positive gradient model (blue in Fig. 5a) results in a *P*-wave velocity at the CMB that is 2.8 per cent faster than in IASP91. The negative gradient model (red) produces a 2.8 per cent slower v_p at the CMB. The absolute gradient values were chosen as plausible regional variations from the global average of IASP91, following Thorne *et al.* (2013), who stated 2.8 per cent as characteristic *S*-velocity variations in D″ (but tomographic models tend to underestimate dv/v, hence we adopted the full 2.8 per cent for dv_p/v_p).

As expected, the fast gradient produces early arrival times compared to IASP91 (blue versus black waveforms in Fig. 5b), and the negative gradient produces delayed arrivals (red versus black waveforms). The advance and delay are 2.2 s and −2.3 s in the lowest frequency band (30 s period), and larger (3–4 s) in the higher frequency bands—this is traveltime dispersion caused by diffraction around the symmetric core. An actually observed Pdiff waveform

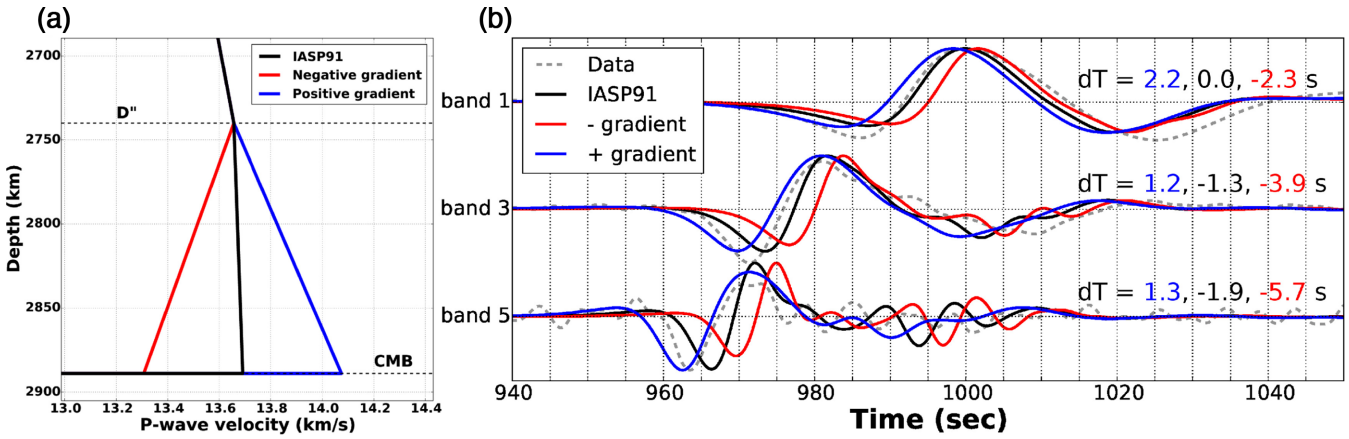

Figure 5. Observed and predicted traveltime dispersions of Pdiff, for different *P*-velocity models of the lowermost mantle. (a) *P*-wave velocities in the D'' layer region according to spherically symmetric reference model IASP91 (black), and two perturbed models featuring linear gradients that result in 2.8 per cent faster velocities at the CMB than IASP91 (blue), or 2.8 per cent slower velocities (red). (b) Observed (dashed) and predicted Pdiff seismograms for a wave path from the example Sumatra event to a station at 131.7° epicentral distance (USArray station J23A, shown in Fig. 6a. This is the blue wave path in Fig. 7a). *Yspec* synthetics were calculated through IASP91 and the two alternative models, and are shown for frequency passbands 1 (dominant period 30.0 s), 3 (15.0 s) and 5 (7.5 s). Traveltime delays $dT = T^{obs} - T^{syn}$ of the observed (dashed) seismograms relative to the synthetics, as computed through the fast model (blue), IASP91 (black), and the slow model (red). A single floating time shift dT_0 between data and synthetics, which is due to uncertainties in absolute earthquake timing, has been arbitrarily fixed such that $dT_{IASP91} = 0$ s in the lowest frequency band, that is, the observed arrival coincides with the IASP91-predicted arrival in this band (which facilitates visual comparison of the waveforms). The observed dT is dispersive: to higher frequencies ($T = 30$, 15 and 7.5 s) the dashed waveform arrives increasingly early ($dT = 0.0$, -1.3 and -1.9 s) w.r.t. IASP91. Comparison to the alternative models suggests a seismically fast wave path—the blue velocity profile produces dispersion of the same sign (increasingly advanced relative to IASP91), although of insufficient magnitude to explain this particular observation. See text for further discussion.

(grey dashed, from the example $M_w = 7.5$ Sumatra event to USArray station J23A, *cf.* map in Fig. 6a) shows the same sign of dispersion as the positive gradient model: increasingly early arrivals as frequency increases. This suggests an anomalously fast wave path in the lowermost mantle, for which IASP91 would be too slow a model—a plausible scenario for a core-grazing path beneath the northern Pacific (the blue path in Fig. 7a), because tomographic models generally infer an anomalously fast lowermost mantle beneath this region (e.g. Woodhouse & Dziewonski 1989; Masters *et al.* 2000; Mégnin & Romanowicz 2000; Grand 2002; Montelli *et al.* 2006; Ritsema *et al.* 2011). The fast anomalies seem to be quite strong judging by the observed dispersion: with increasing frequency, the relative dT advance of the observed seismogram (dashed) w.r.t. to IASP91 is larger than for the fast gradient model (blue waveforms) w.r.t IASP91.

Fig. 6 investigates the magnitude of Pdiff traveltime dispersion that cannot be explained by spherically symmetric structure and must be due to 3-D heterogeneity, using a cluster of stations in the vicinity of station J23A just discussed. Traveltime measurement results of our processing scheme are shown for a set of 30 spatially neighbouring USArray stations that recorded the $M_w = 7.5$ Sumatra event. The 30 stations subdivide into 5 parallel lines {J, L, M, O, R}, each at constant latitude and featuring a station spacing of ≈70 km (Fig. 6a). Most wave paths yielded sufficiently high cross-correlation coefficients for dT results to be considered robust in at least the lower six frequency bands, from $T_d = 30.0$ s to 5.3 s period—Fig. 6(b).

The traveltime anomalies dT in Fig. 6(c) vary significantly across neighbouring stations—this could be mantle, crustal, or near-source effects. But the dT vary almost equally strongly with frequency—a colour change within a row indicates frequency dispersion and hence laterally heterogeneous 3-D structure somewhere on the wave path (rather than diffractive dispersion from the spherically symmetric core). 30 s to 7.5 s is a frequency window where dispersion is not expected to be dominated by reverberations in sediments (Zhou *et al.* 2003) or finite-frequency effects of heterogeneous crust (Ritsema *et al.* 2009) and should thus represent 'useful' signal for mantle tomography. Frequency dependence of dT due to wave propagation in the crust is not modelled because we apply ray-theoretical crustal corrections, but the expected error is small. In continental crust of 35–45 km thickness beneath the stations in Fig. 6 (Bassin *et al.* 2000), the difference between ray-theoretical and true traveltime in the crust is predicted to be less than 0.1 s for the short wave periods ($T < 30$ s) used here (Ritsema *et al.* 2009). Unmodelled dT variations across neighbouring stations, which sit on similar crust, would be even smaller.

The observed frequency dependence of Pdiff traveltimes in Fig. 6 is relatively strong compared to the typical 0.1–0.3 s observed for teleseismic *P* waves in this period range (Sigloch & Nolet 2006). This suggests a significant contribution from heterogeneities in the lowermost mantle. To investigate further, Fig. 7 compares frequency-dependent dT recordings on USArray from two earthquakes at almost identical backazimuths: Event 1 at core-diffracted distance, Event 2 at teleseismic distance. Pdiff traveltime patterns in Fig. 7(b) resemble teleseismic traveltime patterns in Fig. 7(c), suggesting an origin mostly in the upper(most) mantle and crust, which are sampled in similar geometries by both wave types.

Stationwise subtraction of dT of Event 2 from Event 1 (Pdiff minus *P*) should thus enhance the non-upper mantle contribution. Indeed the differential dT pattern in Fig. 7(d) is quite different. The systematic north–south gradient (green to red), more or less parallel to the event backazimuth and 'banded' with epicentral distance, which may indicate that our spherically symmetric reference model needs adjustment, or may be a signature of the elliptic earth (the dT have been corrected for ellipticity, though technically not completely correct for core-grazing waves (Kennett & Gudmundsson 1996)). However, the pattern in Fig. 7(d) is not exclusively banded

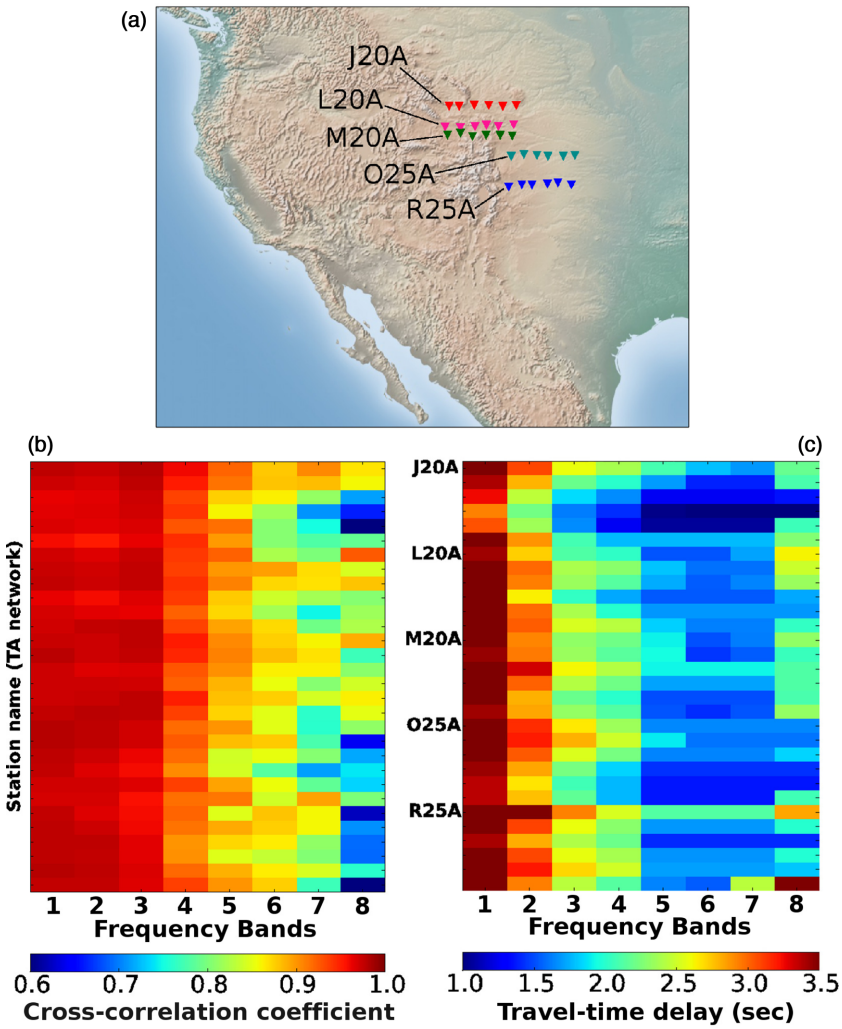

Figure 6. Example traveltime dispersion patterns for Pdiff waves, observed on a cluster of neighbouring USArray stations for the Sumatra event of Fig. 1. (a) 30 spatially neighbouring USArray stations grouped as five linear sub-arrays of constant latitudes J, L, M, O, R. (b) Each pixel shows the cross-correlation coefficient x_c (in colour) for one finite-frequency measurement. Stations in the same sub-array are grouped in neighbouring matrix rows. Most stations (30 rows) and frequency bands (8 columns) yielded measurements of sufficiently high quality ($x_c \geq 0.8$) for an interpretation of traveltime anomalies to be meaningful. The centre periods of frequency bands 1 to 8 are (in seconds): 30.0, 21.2, 15.0, 10.6, 7.5, 5.3, 3.7, 2.7. (c) Traveltime delays dT in seconds. A change of colour *within a row* indicates a frequency-dispersive wave path. Patterns that change from row to row cannot exclusively reflect a biased reference model and must be partly due to 3-D heterogeneity somewhere along the wave path. A lowermost mantle contribution is suspected because the dispersion here exceeds the 0.1–0.3 s typically observed for teleseismic *P* waves by Sigloch & Nolet (2006). However, the columnwise 'banded' structure of very large delays in the lowest bands is probably due either to IASP91 being a biased reference model (*cf.* Fig. 5) or to imperfect ellipticity corrections for the Pdiff arrivals.

and contains additional 3-D signature, presumably of lower-mantle origin.

The last two panels show traveltime dispersion, where dT measured in the 30 s band is subtracted from dT in the 15 s band. Fig. 7(e) shows this for the diffracted data of Event 1, that is, $dT(\text{Pdiff}; T_d = 30\,s) - dT(\text{Pdiff}; T_d = 15\,s)$, and Fig. 7(f) for the teleseismic Event 2, that is, $dT(P; T_d = 30\,s) - dT(P; T_d = 15\,s)$. Such dispersion arises because wave sensitivity to mantle structure is frequency dependent (the size of the Fresnel zone relative to structural anomalies changes). Again the dT dispersion patterns should be similar if due to upper mantle structure, which is sensed similarly by both wave types, and different if caused by 3-D heterogeneities deeper down. The dispersion observations are seen to resemble each other in some aspects, but substantially differ in others (e.g. red in California for Pdiff, blue for P). Also note the larger magnitude of dispersion (more intense colours) for Pdiff than for *P*. Hence, beyond the known, strongly dispersive signature of the *upper* mantle under USArray (Sigloch & Nolet 2006; Sigloch 2008), there seems to be a clear lower-mantle signature present to be exploited by Pdiff-tomography.

3 GLOBAL DATA SET OF MULTIFREQUENCY PDIFF AND *P* TRAVELTIME MEASUREMENTS

We present the global data set of *P*-diffracted and teleseismic *P*-wave dT anomalies assembled so far, and assess the factors that determine measurement success: mainly source–receiver distance, source magnitude and frequency band. Measurement success is defined as the cross-correlation coefficient x_c between observed and synthetic waveforms exceeding $x_c \geq 0.8$—a heuristic value obtained from earlier multifrequency inversions (Sigloch *et al.* 2008; Tian *et al.* 2009).

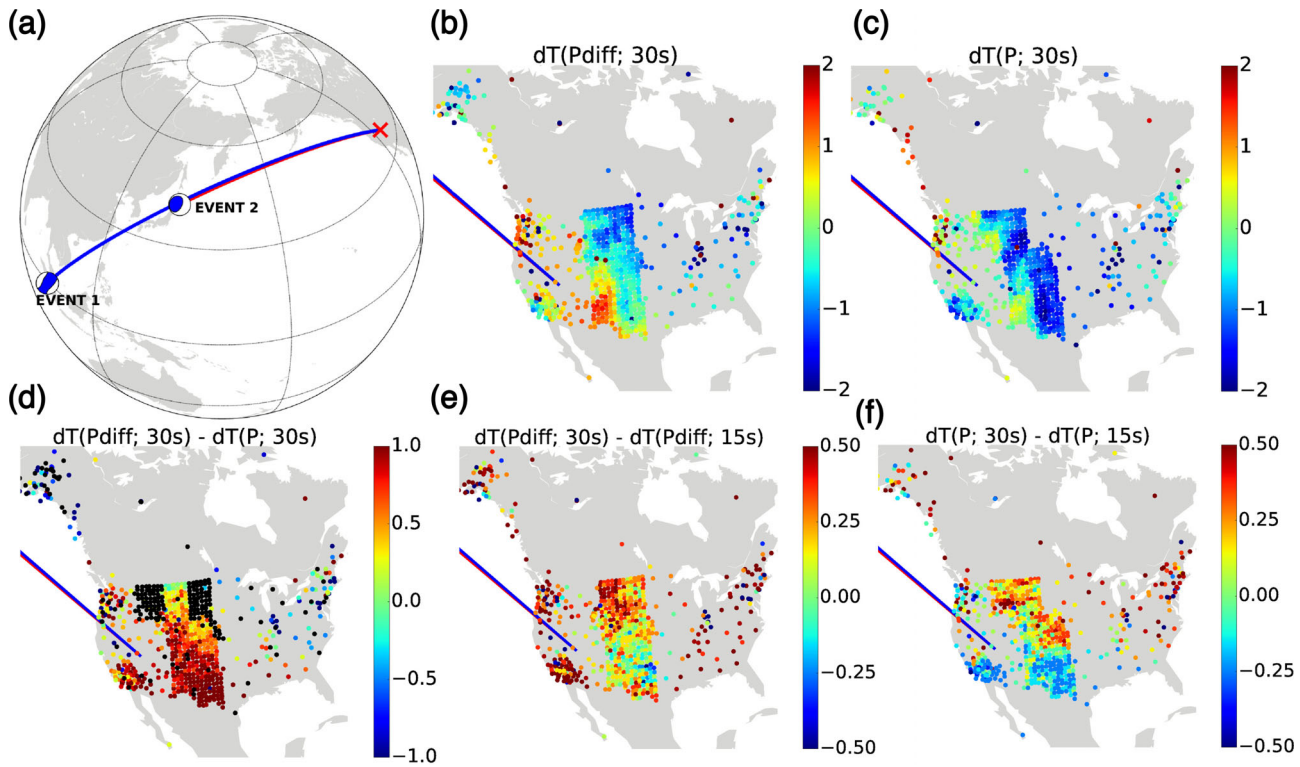

Figure 7. The signature of the lowermost mantle in traveltime measurements. (a) Comparison of two events at almost identical backazimuths from USArray. Event 1 occurred at core-diffracted distances (Southern Sumatra, Indonesia, 2009/09/30 10:16:09.25, 0.72°S, 99.87°E, 82 km depth, 7.5 M_w). Event 2 occurred at teleseismic distances (Hokkaido, Japan region, 2009/06/05 03:30:33.06, 41.82°N, 143.45°E, 28 km depth, 6.4 M_w). Panels (b)–(f) plot dT anomalies in seconds as coloured dots (note that the colour scale changes from panel to panel). Stations lacking data for one event or the other are marked in black. Corrections for ellipticity, crust and station elevation were applied. (b) Event 1, Pdiff traveltime anomalies in the lowest frequency band: $dT(\text{Pdiff}; T_d = 30\,s)$. (c) Event 2, P anomalies in the lowest frequency band: $dT(P; T_d = 30\,s)$. (d) Differential traveltimes in the lowest frequency band: $dT(\text{Pdiff}; T_d = 30\,s) - dT(P; T_d = 30\,s)$. This should subtract out most upper-mantle contributions. (e) Event 1, traveltime dispersion for Pdiff: $dT(\text{Pdiff}; T_d = 30\,s) - dT(\text{Pdiff}; T_d = 15\,s)$. (f) Event 2, traveltime dispersion for P: $dT(P; T_d = 30\,s) - dT(P; T_d = 15\,s)$.

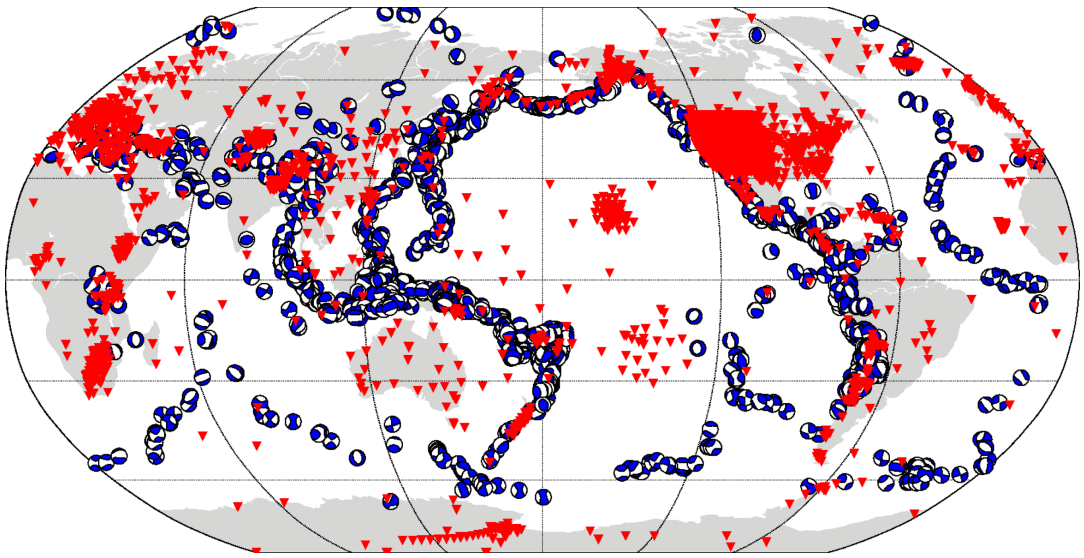

Figure 8. Global distribution of the 1857 earthquake sources (blue beachballs) and 4085 broad-band receivers (red triangles) used in this study. Each source and receiver contributed to at least one successful measurement ($x_c \geq 0.8$) in at least one frequency band. For each source, a broad-band source time function was deconvolved from the waveform data.

Fig. 8 shows the 1857 events and 4085 broad-band stations that contributed at least one usable measurement. 418 226 unique source–receiver paths for Pdiff yielded 479 559 successful, band-passed Pdiff traveltime measurements. 613 057 unique paths for teleseismic P yielded 2 306 755 usable P-wave traveltimes. Source and receiver coverage reflects our 'No data left behind' philosophy, in that we considered every event of magnitude $m_b \geq 5.8$ that occurred between 1999 and 2010—plus many earlier or smaller

events if they occurred in unusual locations. Work is ongoing on the most recent years, as the deconvolution of source time functions still requires human supervision.

The large volumes of broad-band waveform data were retrieved from the IRIS and ORFEUS data management centres using fully automated Python software built for this purpose: *ObsPyLoad* and its successor *obspyDMT*, freely available at http://kasra-hosseini.github.io/obspyDMT, last accessed 17 August 2015 (hosted in *GitHub*, a community-standard repository) and described in Scheingraber *et al.* (2013). *obspyDMT* also executed the instrument correction to ground displacement, bandpass-filtering between 0.01 and 3.5 Hz, local archiving and updating of the collection when new waveforms became available on the IRIS and ORFEUS servers.

Green's functions for the 1857 events, in the broad spectrum of 0.2 mHz to 1 Hz and of 85 min duration, were computed with the *Yspec* software including attenuation (Al-Attar & Woodhouse 2008). Per event, this took about 20 hr on 24 cores (480 core-hours). These Green's functions were convolved with source time functions for the 1857 events, obtained by the linearized method of Sigloch & Nolet (2006).

3.1 Measurement success as a function of epicentral distance, source magnitude and frequency band

Fig. 9 shows histograms of the cross-correlations achieved in *P* versus Pdiff measurements. High cross-correlations are more often achieved in the low-frequency passbands. This is true for both *P* and Pdiff, but significantly more pronounced for Pdiff, as expected from its frequency-dependent attenuation properties of Fig. 2.

At the chosen quality threshold of $x_c \geq 0.8$, the fewest successful *P* measurements are made in the highest frequency band, whereas the fewest successful Pdiff measurements are made at dominant periods around 7.5 s, the band of the secondary microseismic noise. This becomes more evident in Fig. 10, which shows the number of successful measurements versus dominant period. For teleseismic *P*, the number increases with dominant period, whereas good Pdiff measurements are least common in the microseismic noise band (shaded yellow) rather than at the shortest periods.

Fig. 11 plots the percentage of successful measurements versus epicentral distance. In the teleseismic range, receiver distance has no significant influence on measurement success. Frequency band has a moderate influence: at the lowest frequencies, about 55 per cent of attempted source–receiver pairs yield a good measurement, but only about 40 per cent in the highest frequency band. By contrast, measurement success in the *P*-diffracted range drops precipitously as receiver distance increases. Frequency band is seen to have a relatively larger influence than for teleseismic *P*: measurement success is 2–3 times better in the lowest bands than in the high or microseismic noise bands. The much lower success with distance mirrors the exponential drop of Pdiff wave amplitude with distance in Fig. 2. Since the level of random noise in a recording is largely independent of epicentral distance, signal-to-noise ratio decreases as distance increases, and observed waveforms tend to become dominated by noise, no longer fitting the synthetics. This also explains the minimum of usable measurements in the microseismic band, where absolute noise levels exceed those in higher or lower frequency bands, so that signal-to-noise ratio drops below usable levels sooner as a function of distance.

Large earthquakes generate large wave amplitudes, and hence we expect a strong positive effect of earthquake magnitude on measurement success for Pdiff—stronger than for teleseismic *P*. Fig. 12 confirms this. Percentage of successful measurements is plotted against source magnitude, separately for receivers in the close (32°–60°) and far (60°–95°) teleseismic ranges, and in the close (95°–120°) and far (>120°) Pdiff ranges. The results for the two teleseismic groups are very similar: about 30–40 per cent of source–receiver pairs yield successful measurements for the weakest events of $M_w = 5.5$ (percentage averaged over all frequency bands). Success rates decrease with event size, but level off at 60 per cent for $M_w = 6.5$, and even drop again for the largest events (because their true source time functions are more complex than accommodated by our simple point source estimates).

The systematics are different for Pdiff: below magnitude $M_w < 6$, only a small fraction of measurements are successful, especially in the far teleseismic range. Measurement success increases strongly with event magnitude, again confirming that Pdiff measurements are limited mainly by signal-to-noise ratio. Magnitude 8 events produce remarkable success ratios of >35 per cent even in the far teleseismic range, which equals the success ratios for teleseismic *P*. In order to achieve >35 per cent good measurements, event magnitudes M_w

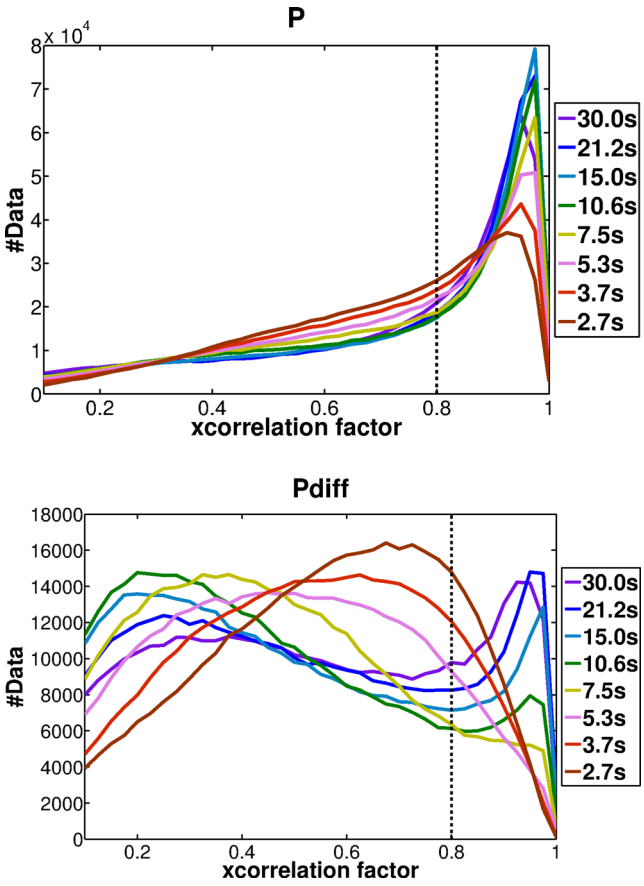

Figure 9. Histograms of measurement success for *P* versus Pdiff. The metric is the cross-correlation coefficient x_c, which from our experience should exceed $x_c \geq 0.8$ in order to be adequate for tomography. Top: histogram of x_c values achieved for teleseismic *P* measurements (distance range 32°–95°) in each of the eight frequency passbands. The values peak well above $x_c > 0.9$, indicating highly likely measurement success. The higher the frequency, the fewer usable measurements are achieved. Bottom: same as top, but for Pdiff waves (distance range 97°–160°). Compared to teleseismic *P*, a much lower fraction of measurements achieves high $x_c \geq 0.8$, especially in the higher frequency bands, where diffraction dramatically lowers the signal-to-noise ratio.

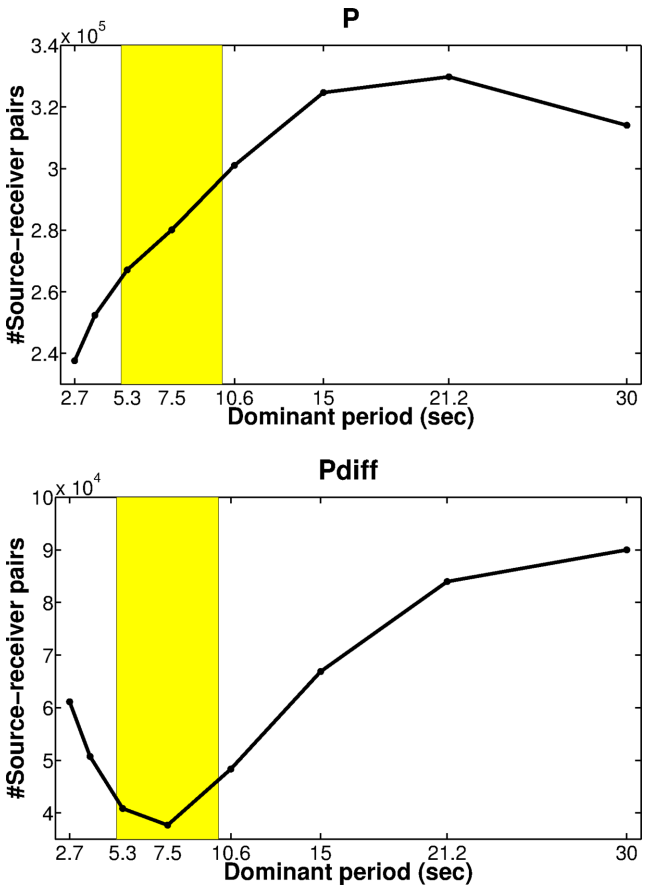

Figure 10. Histograms of satisfactory *P* and Pdiff measurements, as a function of frequency band. A measurement is included only if it achieved cross-correlation coefficient $x_c \geq 0.8$. Yellow shading marks the secondary microseismic noise band. Top: for teleseismic *P* waves, measurement success increases (almost) monotonously with wave period. Bottom: for Pdiff waves, measurement success is lowest in the band of the secondary microseismic noise.

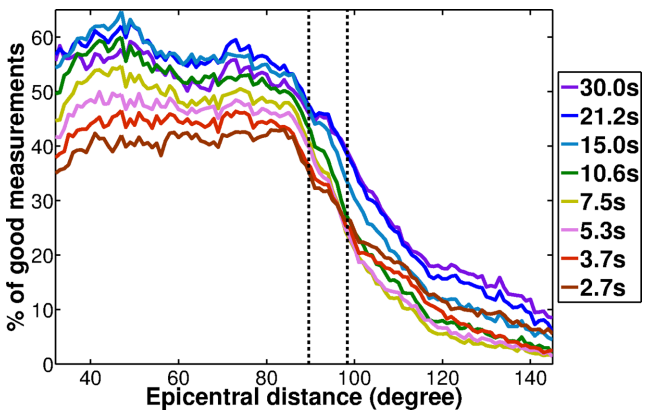

Figure 11. Percentage of successful dT measurements ($x_c \geq 0.8$), as a function of epicentral distance and frequency band. In the teleseismic *P* range, measurement success depends more on the frequency band than on epicentral distance, and varies between 55 and 40 per cent in the lowest and highest bands, respectively. In the *P*-diffracted range, measurement success rate drops sharply with increasing distance, mirroring the exponential drop in signal amplitudes of Fig. 2. Success rate is lowest in the secondary microseismic noise band (yellow and pink lines, consistent with Fig. 10).

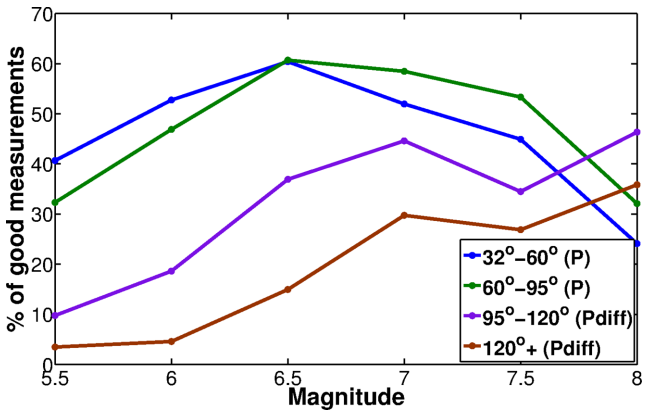

Figure 12. Percentage of successful dT measurements ($x_c \geq 0.8$), as a function of earthquake source magnitude M_w and epicentral distance range. In the core-diffracted range (red and purple lines), the rate of successful measurements grows with earthquake magnitude. In the teleseismic *P* range (green and blue), this is only true for small magnitudes ($M_w < 6.5$). For larger events the success rate drops again, because our point-source approximation becomes inadequate.

must be approximately 5.5, 5.7, 6.5 and 8.0 for the near-P, far-P, near-Pdiff and far-Pdiff ranges, respectively.

Fig. 13 shows histograms of measured traveltime anomalies dT in the *P* versus Pdiff ranges, sorted by frequency band (colours). The dT are corrected for the earth's ellipticity, for station topography, and for crustal structure using crustal model CRUST2.0 (Bassin *et al.* 2000). Standard deviations range between 1.44 s and 2.14 s for teleseismic dT (depending on frequency band), and between 1.92 s and 3.94 s for *P*-diffracted dT. The relative differences between frequency bands and distance ranges are real, but the absolute dT values are conservative estimates because the mean of the dT has been removed eventwise. A non-zero mean could result from a misestimated origin time rather than from 3-D structural heterogeneity, the signal of interest. On the other hand, removing the mean may discard some signal that is truly due to earth structure, hence 'conservative'. The mean was not calculated on all measurements—this would yield decidedly non-Gaussian histograms because the mean would be skewed by a few spatially concentrated station clusters, mainly USArray. Instead it was calculated on the rather evenly distributed Global Seismographic Network in the lowest frequency band, and subsequently removed from the dT values of all stations and all bands, yielding the largely Gaussian histograms of Fig. 13.

3.2 Global mantle heterogeneity inferred from Pdiff traveltime anomalies

We turn to the structural information contained in our large, global set of *P*-diffracted traveltime data. Out of 418 226 candidate Pdiff source–receiver paths, 165 651 yielded at least one successful passband measurement. 3 345 808 attempts at measurements (418 226 paths times 8 frequency bands) yielded 479 559 multifrequency dT values of $x_c \geq 0.8$. The dTs are corrected for the effects of ellipticity, crust and station elevation.

Fig. 14 plots the coverage of the CMB by nominally core-grazing segments of 479 559 Pdiff paths that yielded successful measurements. Showing the Fresnel zones of finite-frequency kernels instead of rays would be a more faithful approximation of true measurement sensitivities near the CMB, but this major computational effort was not complete at the time of writing. The CMB was subdivided into blocks of 0.5°, that is, 720 × 720 blocks, and for each block, the lengths of all core-grazing segments visiting it are

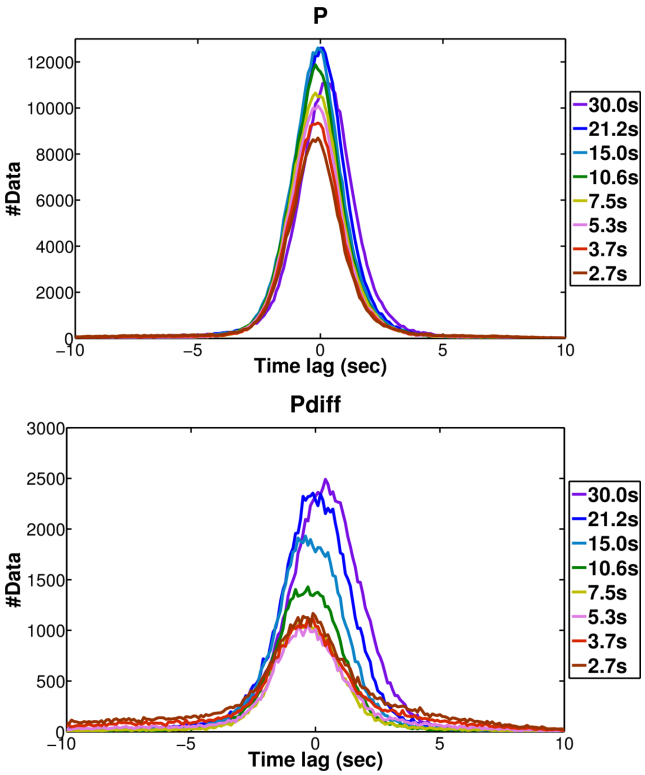

Figure 13. Histograms of multifrequency traveltime anomalies dT. The mean of dT was removed eventwise, and topographic, crustal and ellipticity corrections were applied. Only measurements that yielded $x_c \geq 0.8$ are included. Top: dT of teleseismic P waves. Their standard deviation σ_T ranges between 1.44 and 2.14 s, depending on frequency band. Bottom: dT of core-diffracted Pdiff waves, with σ_T ranging between 1.92 and 3.94 s.

summed up, yielding a measure of how well each block is sampled. This is equivalent to plotting the cumulative column density (sum over each column) of an inversion matrix.

The lowermost mantle under the northern Pacific and East Asia are most densely sampled (dark red). The oceans of the southern hemisphere, especially the southern Atlantic, are the most poorly sampled. Overall, however, the lowermost mantle is better sampled under the oceans than under the continents. The heavy footprint of USArray appears as localized, red–yellow patches, with the clearest example located under South America and the adjacent Pacific (from paths that originate from seismicity in South Sandwich). Fig. 14 also permits to gauge the extent to which wave paths cross, an important proxy for tomographic resolution.

Fig. 15 shows the same ray coverage as Fig. 14, but projected on the CMB are traveltime anomalies dT, permitting to assess the spatial distribution of seismically fast and slow regions in the lowermost mantle. This rough 'proto-tomography' exercise assumes that all arrival delays or advances originate from the core-grazing path segments. Each ray segment is coloured by the relative traveltime delay incurred w.r.t. the reference velocity model IASP91 and the Q values of PREM. Red paths are seismically slow, blue paths are fast. Anomalies are seen to be on the order of 1 per cent.

Large-scale structures emerge that are well-known from global tomography models, such as generally slow regions beneath the southern hemisphere, corresponding to the African and Pacific Large Low Shear Velocity Provinces (LLSVPs). Seismically fast areas are confirmed under most of eastern Asia and under Central America, presumably the resting places of massive accumulations of subducted lithosphere. A striking east-west velocity gradient is evident across the USArray-sampled patch beneath South America and adjacent Pacific (compare to Fig. 14). Other strong velocity gradients appear to rim the Pacific LLSVP.

4 DISCUSSION

For waveform measurements on Pdiff waves, the main challenge is their signal-to-noise ratio. Wave amplitudes that rapidly decline with epicentral distance and with frequency (Figs 2 and 11) meet with ambient noise levels that peak in the microseismic frequency band. Our approach mitigates by attempting measurements in 8 different passbands across the broad-band range of 30.0–2.7 s period, maximising the chance that at least one measurement will succeed, so that the wave path is basically covered. Fitting a passband waveform is easier than a broad-band measurement, since the latter depends on good SNR across all frequencies. This is particular pertinent in selectively high-noise environments, as for Pdiff waves or on the ocean floor (where signal is not weak *per se*, but microseismic noise is elevated compared to land stations).

Over all eight bands and all distances, 14.3 per cent (479 559) high-quality, multifrequency Pdiff measurements were achieved, compared to 47.0 per cent (2 306 755) teleseismic P measurements. Diffracted P-wave measurements are most likely to succeed in the lowest frequency band of 30.0 s period (21.5 per cent success rate) and least likely in the 7.5 s period band of the microseismic noise (9.0 per cent). Successful teleseismic P measurements are most likely at 21.2 s (53.8 per cent) and least likely in the highest band of 2.7 s (38.8 per cent).

For a given wave path, the frequency dispersion between dT at the low and high ends of our frequency range can be 1–2 s, although more of this seems to be due to a mismatch of the spherically symmetric reference model rather than to 3-D heterogeneity (Fig. 6). Nevertheless, the signature of 3-D mantle heterogeneity is clearly present in Figs 6 and 7. A substantial part of this signal seems to originate from the lowermost mantle, since dT dispersion is significantly stronger for Pdiff than for P.

Computing Green's functions and sensitivity kernels up to the high frequencies used here is challenging and currently only feasible in a spherically symmetric reference model. This limitation may not be a serious one, given that mantle heterogeneity is expected to be of only a few percent, except perhaps in Ultra-Low Velocity Zones (ULVZs), which are however very limited spatially. Hence a single-iteration matrix inversion, starting from a spherically symmetric reference model, should be capable of yielding a very good approximation to true earth structure. We hope and expect that our ability to exploit the highly resolving short wavelengths will far outweigh the limitation of not being able to iteratively update the solution.

The *Yspec* and *AxiSEM* software packages tools are both capable of delivering accurate Green's functions in spherically symmetric reference models, for the ambitious, broad-band frequency range in this study. Since *AxiSEM* was not complete at the time of creating our synthetic archive, *Yspec* was used to calculate all the traces in ≈2000 events of our data set which cost $\approx 10^6$ CPU hours in total. We intend to adapt the work flow to incorporate the *Instaseis* database approach of van Driel *et al.* (2015). This expends a large upfront effort on computing and storing generic global Green's functions componentwise using databases generated by *AxiSEM*. Extraction from the database and linear combination into specific Green's functions then becomes quasi instantaneous (on the order of milliseconds). Sensitivity kernels from full forward and backward

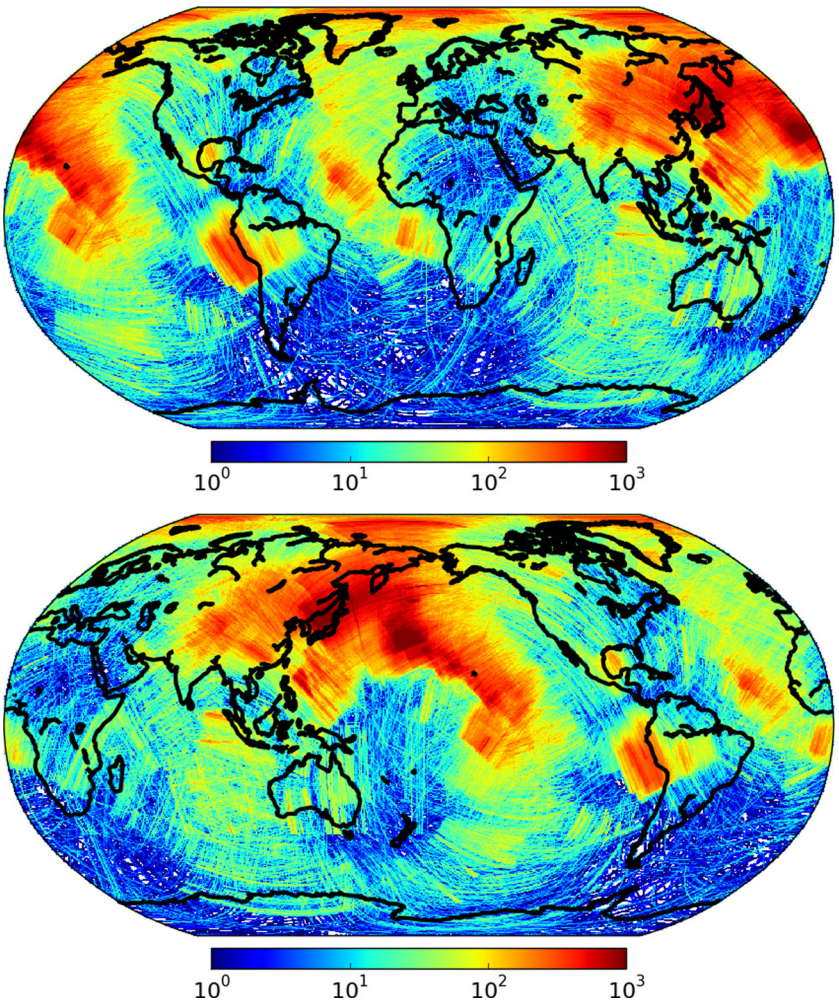

Figure 14. Sampling of the lowermost mantle by our data set of 479 559 Pdiff traveltime anomalies. The same data are shown in two different map views, Atlantic-centred at the top, Pacific-centred at the bottom. Each line represents the core-grazing segment of a ray-theoretical Pdiff path that yielded a successful measurement (i.e. $x_c \geq 0.8$ in any frequency band). Density of ray path coverage is indicated by colours (note that the colour scale is logarithmic). The CMB under oceans tends to be better sampled than under continents, especially in the southern hemisphere. The true sensitivity of a Pdiff wave to core–mantle boundary structure is ellipsoidal rather than ray-like—covering a broader area of the CMB and extending hundreds of kilometres into the overlying mantle.

wavefields will also be computed with *AxiSEM*, since *Yspec* is not an efficient tool for this purpose.

Deconvolution of source parameters is the bottleneck that requires the most user supervision, and no earthquake centre currently does this work. Stähler & Sigloch (2014) demonstrated a scheme of probabilistic inference that should largely automate this step. It also delivers full source uncertainty estimates and propagates them into the (correlated) uncertainties of dT measurements, as required to properly fill the measurement covariance matrix for tomography.

In terms of structural heterogeneity at long spatial wavelengths, the results of Fig. 15 are encouragingly consistent with prior studies that used different methods and data. This includes the aforementioned LLSVPs and the slab graveyards under Eastern Asia and Central America, which have become robust features in global tomographic models, especially *S*-wave models, such as S362ANI (Kustowski *et al.* 2008), S40RTS (Ritsema *et al.* 2011), SAW24B16 (Mégnin & Romanowicz 2000), HMSL-S (Houser *et al.* 2008), or GyPSuM (Simmons *et al.* 2010). Because *P*-wave models do not have the benefit of including normal modes, their resolution of lowermost mantle structure is generally considered less reliable and more attenuated. While too early to assess the improvements possible through Pdiff in this regard, the large number of successful Pdiff measurements and their general agreement with known structure is promising.

Since the pioneering studies of Wysession (1996) and Kàrason & Van der Hilst (2001), Pdiff waves have not been explicitly included in global *P*-wave tomographies. Both studies used a data set of 543 PKPdf - Pdiff differential traveltimes. By comparison, we obtained 479 559 usable Pdiff waveform measurements, demonstrating the sea change in data availability that has taken place. While our structural findings bear more overall resemblance to recent global *S*-wave models, they are also broadly consistent with these two early, global Pdiff inversions, which recovered the two LLSVPs as well as high-velocity anomalies beneath south/central America and eastern Asia. Not present in our dT map is a high velocity structure under south and southeast of Africa that was apparently required by their Pdiff data in both the Wysession (1996) and the Kàrason & Van der Hilst (2001) study.

From Pdiff measurements made by Ritsema & van Heijst (2002), Koelemeijer *et al.* (2013) constructed a traveltime map similar to our Fig. 15, by projecting the entire dT anomalies onto the CMB. With a coarse gridding of 5° caps, only large-scale structure was targeted.

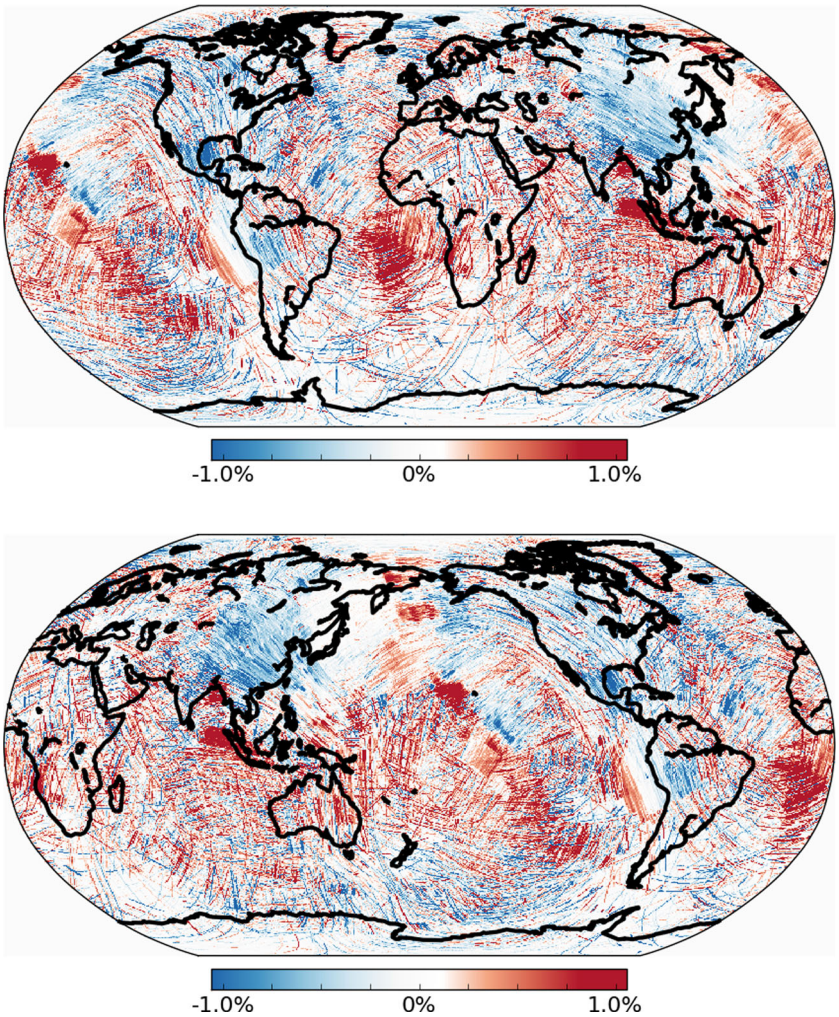

Figure 15. Traveltime anomalies of 479 559 Pdiff waves, projected onto their CMB-grazing segments. As Fig. 14, except that colour represents the traveltime anomaly *dT* in per cent. Red designates a measurement delayed relative to IASP91, blue means advanced. For a given delay *dT*, a longer core-grazing segment would result in a fainter shade of red, because *dT* is spread evenly along the segment. The raw *dT* measurements were corrected for earth's ellipticity, station topography and near-station crustal structure. Assuming that most Pdiff traveltime anomalies originate in the lowermost mantle, this plot represents a rough 'proto-tomography', charting out seismically fast (blue) and slow (red) structural anomalies near the CMB.

They recovered the two LLSVPs and high-velocity anomalies under central America and east Asia—another confirmation of these most robust features in the lowermost mantle.

A relatively small-scale but pronounced feature of Fig. 15 is an intensely slow patch just west of Hawaii. This structure was recently described as a newly recognized ULVZ by Cottaar & Romanowicz (2012), who modelled Sdiff waveforms. It appears to be highly visible to *P* waves as well.

5 CONCLUSION

We presented a method to routinely measure and model core-diffracted *P* waves across the broad-band frequency range. Green's functions are calculated by semi-analytical (i.e. theoretically exact) wave propagation through a spherically symmetric reference model, to 1 Hz dominant frequency, and broad-band source time functions are deconvolved from the waveform data. Largely automated processing of 1857 events yielded 2 306 755 teleseismic *P*- and 479 559 *P*-diffracted traveltime measurements by cross-correlation across eight frequency bands (dominant periods 30–2.7 s).

While significantly more challenging than teleseismic *P*-measurements, we obtain very decent success rates for *dT* measurements on Pdiff waveforms, of around 14 per cent across all attempted wave paths and frequencies. The main challenge is signal-to-noise ratio, which drops precipitously with epicentral distance and with frequency, as expected for diffracted waves. *dT* anomalies are larger for Pdiff than for *P* waves, and frequency dependence of *dT* due to 3-D heterogeneity is stronger for Pdiff as well. Projected on their core-grazing ray segments, the *dT* measurements recover major structural, lower-mantle heterogeneities known from existing global mantle models based on *P*- and *S* waves. This methodically novel and very large data set of core-diffracted *P* waves is ready for global waveform tomography.

ACKNOWLEDGEMENTS

We thank David Al-Attar, Jeroen Ritsema, and editor Gabi Laske for their careful and constructive reviews. We are grateful to David Al-Attar for discussions and assistance with his *Yspec* software, and to Tarje Nissen-Meyer for help with his *AxiSEM* software. All waveform data came from the IRIS and ORFEUS

data management centres, and were downloaded and managed using the obspyDMT software package, freely available at http://kasra-hosseini.github.io/obspyDMT (last accessed 17 August 2015). K.H. was funded by Deutsche Forschungsgemeinschaft (DFG) grants made to K.S., grant numbers SI 1538/1-1 (in Priority Programme SAMPLE) and SI 1538/2-1 (project RHUM-RUM).

REFERENCES

Aki, K. & Richards, P.G., 2002. *Quantitative Seismology,* University Science Books.

Al-Attar, D. & Woodhouse, J.H., 2008. Calculation of seismic displacement fields in self-gravitating earth models–applications of minors vectors and symplectic structure, *Geophys. J. Int.,* **175**(3), 1176–1208.

Bassin, C., Laske, G. & Masters, G., 2000. The current limits of resolution for surface wave tomography in North America, *EOS, Trans. Am. geophys. Un.,* **81,** F897.

Chapman, C., 1978. A new method for computing synthetic seismograms, *Geophys. J. R. astr. Soc.,* **54,** 481–518.

Cottaar, S. & Romanowicz, B., 2012. An unsually large ULVZ at the base of the mantle near Hawaii, *Earth planet. Sci. Lett.,* **355,** 213–222.

Dahlen, F.A., Hung, S.-H. & Nolet, G., 2000. Fréchet kernels for finite-frequency traveltimes-I. Theory, *Geophys. J. Int.,* **141**(1), 157–174.

Dziewonski, A.M. & Anderson, D.L., 1981. Preliminary reference Earth model, *Phys. Earth planet. Inter.,* **25,** 297–356.

Fichtner, A., Igel, H., Bunge, H.-P. & Kennett, B.L.N., 2009. Simulation and inversion of seismic wave propagation on continental scales based on a spectral-element method, *Journal of Numerical Analysis, Industrial and Applied Mathematics,* **4**(1–2), 11–22.

Friederich, W. & Dalkolmo, J., 1995. Complete synthetic seismograms for a spherically symmetric Earth by a numerical computation of the Green's function in the frequency domain, *Geophys. J. Int.,* **122,** 537–550.

Fuchs, K. & Müller, G., 1971. Computation of synthetic seismograms with the reflectivity method and comparison with observations, *Geophys. J. R. astr. Soc.,* **23,** 417–433.

Grand, S.P., 2002. Mantle shear–wave tomography and the fate of subducted slabs, *Phil. Trans. R. Soc. A,* **360**(1800), 2475–2491.

Hafkenscheid, E., Wortel, M.J.R. & Spakman, W., 2006. Subduction history of the Tethyan region derived from seismic tomography and tectonic reconstructions, *J. geophys. Res.,* **111**(B8), doi:10.1029/2005JB003791.

Hosseini-zad, K., Stähler, S.C., Sigloch, K. & Scheingraber, C., 2012. "No data left behind": efficient processing of large datasets for waveform tomography and Bayesian source inversion, in *EGU General Assembly 2012,* held 2012 April 22–27 in Vienna, Austria, p. 4157.

Houser, C., Masters, G., Shearer, P. & Laske, G., 2008. Shear and compressional velocity models of the mantle from cluster analysis of long-period waveforms, *Geophys. J. Int.,* **174,** 195–212.

Kàrason, H. & Van der Hilst, R.D., 2001. Tomographic imaging of the lowermost mantle with differential times of refracted and diffracted core phases (PKP, Pdiff), *J. geophys. Res.,* **106,** 6569–6587.

Kennett, B.L.N. & Engdahl, E.R., 1991. Traveltimes for global earthquake location and phase identification, *Geophys. J. Int.,* **105,** 429–465.

Kennett, B.L.N. & Gudmundsson, O., 1996. Ellipticity corrections for seismic phases, *Geophys. J. Int.,* **127**(1), 40–48.

Knopoff, L. & Gilbert, F., 1961. Diffraction of elastic waves by the core of the earth, *Bull. seism. Soc. Am.,* **51**(1), 35–49.

Koelemeijer, P., Deuss, A. & Ritsema, J., 2013. Observations of core-mantle boundary Stoneley modes, *Geophys. Res. Lett.,* **40,** 2557–2561.

Komatitsch, D. & Tromp, J., 2002a. Spectral-element simulations of global seismic wave propagation—I. Validation, *Geophys. J. Int.,* **149,** 390–412.

Kustowski, B., Ekström, G. & Dziewonski, A.M., 2008. Anisotropic shear-wave velocity structure of the Earth's mantle: a global model, *J. geophys. Res.,* **113**(B6), 2156–2202.

Li, C., van der Hilst, R.D., Engdahl, E.R. & Burdick, S., 2008. A new global model for P wave speed variations in Earth's mantle, *Geochem. Geophys. Geosyst.,* **9**(5), doi:10.1029/2007GC001806.

Liu, Q. & Tromp, J., 2008. Finite-frequency sensitivity kernels for global seismic wave propagation based upon adjoint methods, *Geophys. J. Int.,* **174,** 265–286.

Masters, G., Laske, G., Bolton, H. & Dziewonski, A., 2000. The relative behavior of shear velocity, bulk sound speed, and compressional velocity in the mantle: implications for chemical and thermal structure, *Earth's Deep Interior: Mineral Physics and Tomography from the Atomic to the Global Scale,* pp. 63–87, eds Karato, S.-I., Forte, A., Liebermann, R., Masters, G. & Stixrude, L., American Geophysical Union.

Mégnin, C. & Romanowicz, B., 2000. The three-dimensional shear velocity structure of the mantle from the inversion of body, surface and higher-mode waveforms, *Geophys. J. Int.,* **143**(3), 709–728.

Mercerat, E.D. & Nolet, G., 2013. On the linearity of cross-correlation delay times in finite-frequency tomography, *Geophys. J. Int.,* **192**(2), 681–687.

Montelli, R., Nolet, G., Dahlen, F.A. & Masters, G., 2006. A catalogue of deep mantle plumes: New results from finite-frequency tomography, *Geochem. Geophys. Geosyst.,* **7**(11), doi:10.1029/2006GC001248.

Nissen-Meyer, T., Dahlen, F.A. & Fournier, A., 2007. Spherical-earth Fréchet sensitivity kernels, *Geophys. J. Int.,* **168,** 1051–1066.

Nissen-Meyer, T., van Driel, M., Stähler, S.C., Hosseini, K., Hempel, S., Auer, L., Colombi, A. & Fournier, A., 2014. AxiSEM: broadband 3-D seismic wavefields in axisymmetric media, *Solid Earth,* **5**(1), 425–445.

Nolet, G. & Dahlen, F.A., 2000. Wave front healing and the evolution of seismic delay times, *J. geophys. Res.,* **105,** 19 043–19 054.

Panning, M. & Romanowicz, B., 2006. A three-dimensional radially anisotropic model of shear velocity in the whole mantle, *Geophys. J. Int.,* **167**(1), 361–379.

Pavlis, G.L., Sigloch, K., Burdick, S., Fouch, M.J. & Vernon, F.L., 2012. Unraveling the geometry of the Farallon plate: synthesis of three-dimensional imaging results from USArray, *Tectonophysics,* **532,** 82–102.

Ren, Y., Stutzmann, E., Van Der Hilst, R.D. & Besse, J., 2007. Understanding seismic heterogeneities in the lower mantle beneath the Americas from seismic tomography and plate tectonic history, *J. geophys. Res.,* **112**(B1), doi:10.1029/2005JB004154.

Ritsema, J. & van Heijst, H., 2002. Constraints on the correlation of P and S-wave velocity heterogeneity in the mantle from P, PP, PPP and PKPab traveltimes, *Geophys. J. Int.,* **149**(2), 482–489.

Ritsema, J., van Heijst, H.J. & Woodhouse, J.H., 2004. Global transition zone tomography, *J. geophys. Res.,* **109**(B2), doi:10.1029/2003JB002610.

Ritsema, J., Van Heijst, H.J., Woodhouse, J.H. & Deuss, A., 2009. Long-period body wave traveltimes through the crust: implication for crustal corrections and seismic tomography, *Geophys. J. Int.,* **179**(2), 1255–1261.

Ritsema, J., Deuss, A., van Heijst, H.J. & Woodhouse, J.H., 2011. S40RTS: a degree-40 shear-velocity model for the mantle from new Rayleigh wave dispersion, teleseismic traveltime and normal-mode splitting function measurements, *Geophys. J. Int.,* **184(3),** 1223–1236.

Sacks, S., 1966. Diffracted wave studies of the Earth's core: 1. Amplitudes, core size, and rigidity, *J. geophys. Res.,* **71**(4), 1173–1181.

Scheingraber, C., Hosseini, K., Barsch, R. & Sigloch, K., 2013. ObsPyLoad: a tool for fully automated retrieval of seismological waveform data, *Seismol. Res. Lett.,* **84**(3), 525–531.

Sigloch, K., 2008. Multiple-frequency body-wave tomography, *PhD thesis,* Princeton University.

Sigloch, K. & Mihalynuk, M.G., 2013. Intra-oceanic subduction shaped the assembly of Cordilleran North America, *Nature,* **496**(7443), 50–56.

Sigloch, K. & Nolet, G., 2006. Measuring finite-frequency body wave amplitudes and travel times, *Geophys. J. Int.,* **167,** 271–287.

Sigloch, K., McQuarrie, N. & Nolet, G., 2008. Two-stage subduction history under North America inferred from multiple-frequency tomography, *Nature Geoscience,* **1,** 458–462.

Simmons, N.A., Forte, A.M., Boschi, L. & Grand, S.P., 2010. GyPSuM: a joint tomographic model of mantle density and seismic wave speeds, *J. geophys. Res.,* **115,** B12310, doi:10.1029/2010JB007631.

Stähler, S.C. & Sigloch, K., 2014. Fully probabilistic seismic source inversion–Part 1: Efficient parameterisation, *Solid Earth,* **5**(2), 1055–1069.

Stähler, S.C., Sigloch, K. & Nissen-Meyer, T., 2012. Triplicated P-wave measurements for waveform tomography of the mantle transition zone, *Solid Earth,* **3**(2), 339–354.

Su, W.-j. & Dziewonski, A.M., 1997. Simultaneous inversion for 3-D variations in shear and bulk velocity in the mantle, *Phys. Earth planet. Inter.,* **100**(1), 135–156.

Thorne, M.S., Zhang, Y. & Ritsema, J., 2013. Evaluation of 1-D and 3-D seismic models of the Pacific lower mantle with S, SKS, and SKKS traveltimes and amplitudes, *J. geophys. Res.,* **118**(3), 985–995.

Tian, Y., Sigloch, K. & Nolet, G., 2009. Multiple-frequency SH-wave tomography of the western US upper mantle, *Geophys. J. Int.,* **178**(3), 1384–1402.

Vallée, M., Charléty, J., Ferreira, A. M.G., Delouis, B. & Vergoz, J., 2011. SCARDEC: a new technique for the rapid determination of seismic moment magnitude, focal mechanism and source time functions for large earthquakes using body-wave deconvolution, *Geophys. J. Int.,* **184**(1), 338–358.

van der Meer, D.G., Spakman, W., van Hinsbergen, D. J.J., Amaru, M.L. & Torsvik, T.H., 2010. Towards absolute plate motions constrained by lower-mantle slab remnants, *Nat. Geosci.,* **3**(1), 36–40.

Van der Voo, R., Spakman, W. & Bijwaard, H., 1999a. Mesozoic subducted slabs under Siberia, *Nature,* **397**(6716), 246–249.

Van der Voo, R., Spakman, W. & Bijwaard, H., 1999b. Tethyan subducted slabs under India, *Earth planet. Sci. Lett.,* **171**(1), 7–20.

van Driel, M. & Nissen-Meyer, T., 2014a. Optimized viscoelastic wave propagation for weakly dissipative media, *Geophys. J. Int.,* **199**(2), 1078–1093.

van Driel, M. & Nissen-Meyer, T., 2014b. Seismic wave propagation in fully anisotropic axisymmetric media, *Geophys. J. Int.,* **199**(2), 880–893.

van Driel, M., Krischer, L., Stähler, S.C., Hosseini, K. & Nissen-Meyer, T., 2015. Instaseis: instant global seismograms based on a broadband waveform database, *Solid Earth,* **6**(2), 701–717.

Woodhouse, J.H., 1980. Efficient and stable methods for performing seismic calculations in stratified media, in *Proc. Enrico Fermi Int. Sch. Phys., Course LXXVIII,* pp. 127–151, Amsterdam, North Holland Publishing Company.

Woodhouse, J.H. & Dziewonski, A.M., 1989. Seismic modelling of the Earth's large-scale three-dimensional structure, *Phil. Trans. R. Soc. A,* **328**(1599), 291–308.

Wysession, M.E., 1996. Large-scale structure at the core-mantle boundary from diffracted waves, *Nature,* **382**(6588), 244–248.

Zhou, Y., Nolet, G. & Dahlen, F.A., 2003. Surface sediment effects on teleseismic P wave amplitude, *J. geophys. Res.,* **108**(B9), doi:10.1029/2002JB002331.